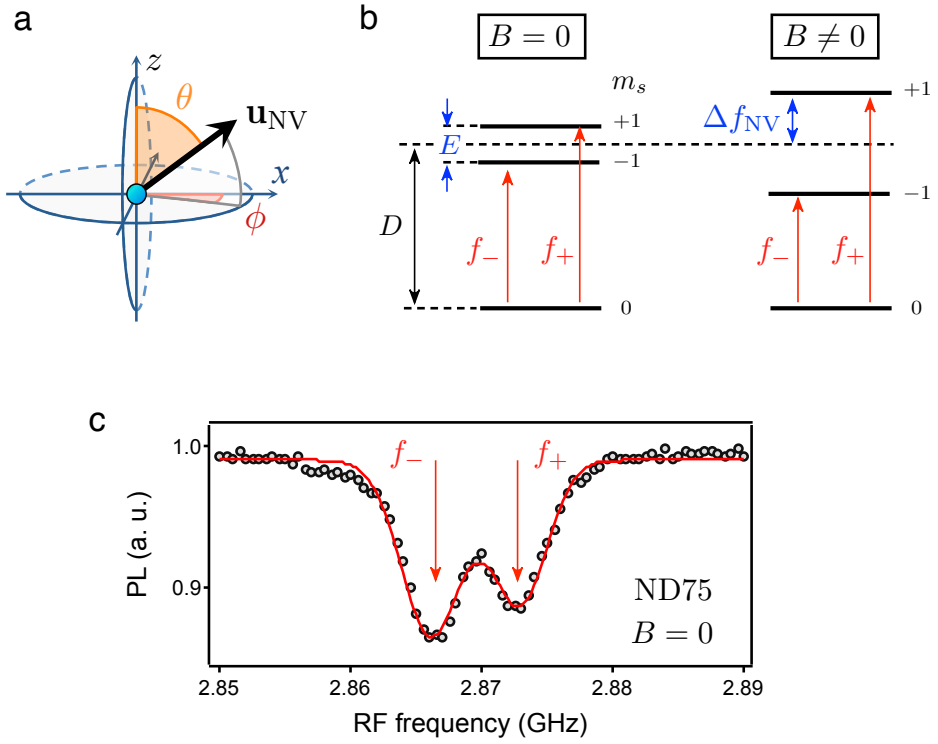

Supplementary Figure 1. Characterization of the magnetic field sensor. (a) The quantization axis $\mathbf{u}_{\mathrm{NV}}$ of the NV center's electron spin is characterized by spherical angles (θ,ϕ) in the (xyz) sample reference frame. (b) Structure of the spin sublevels in the NV defect's ground state. The ESR frequencies corresponding to the electron spin transitions $m_s = 0 \rightarrow -1$ and $m_s = 0 \rightarrow +1$ are denoted by f_- and f_+, respectively. (c) ESR spectrum of ND75 in zero external magnetic field. A fit to a sum of two Gaussian functions allows determining the parameters D and E that characterize the NV center. The values are given in Supplementary Table 1.

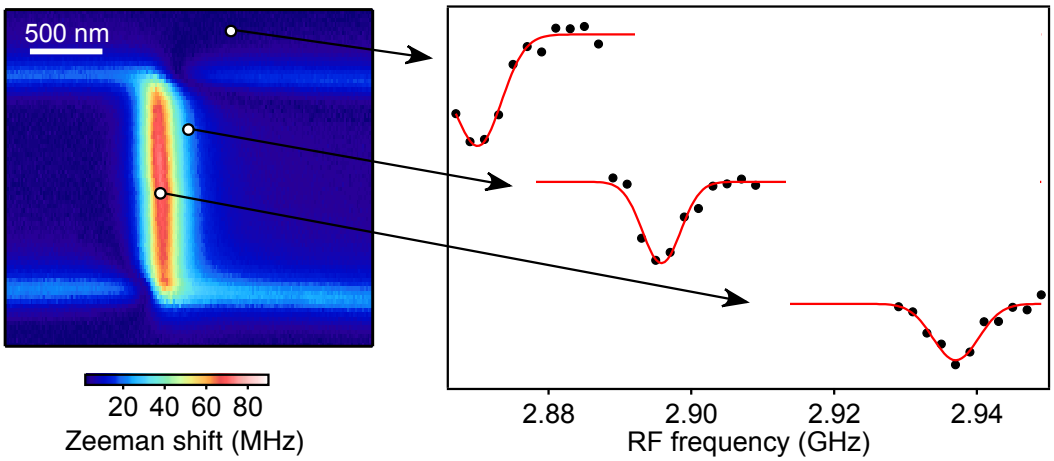

Supplementary Figure 2. Quantitative stray-field imaging with a scanning-NV defect. Map of the Zeeman shift Δf_{NV} obtained with ND74d above the domain wall (reproduced from Fig. 3b of the main paper), along with the raw ESR spectra corresponding to 3 different selected pixels. Solid lines are Gaussian fits.

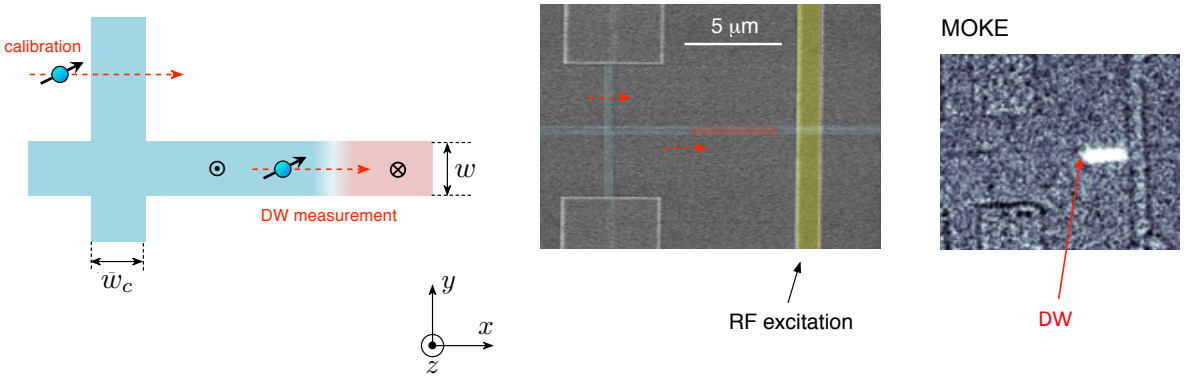

Supplementary Figure 3. Geometry of the ferromagnetic samples. The samples were patterned into two perpendicular wires, one of width w_c used for the calibration, the other of width w for the DW study. Left panel: Schematic of the sample. Middle panel: Scanning electron micrograph of the Ta/CoFeB/MgO sample, showing in color the magnetic domains (up in blue, down in red) and the RF antenna (yellow). Right panel: Magneto-optical Kerr microscopy image of the Ta/CoFeB/MgO sample after nucleation.

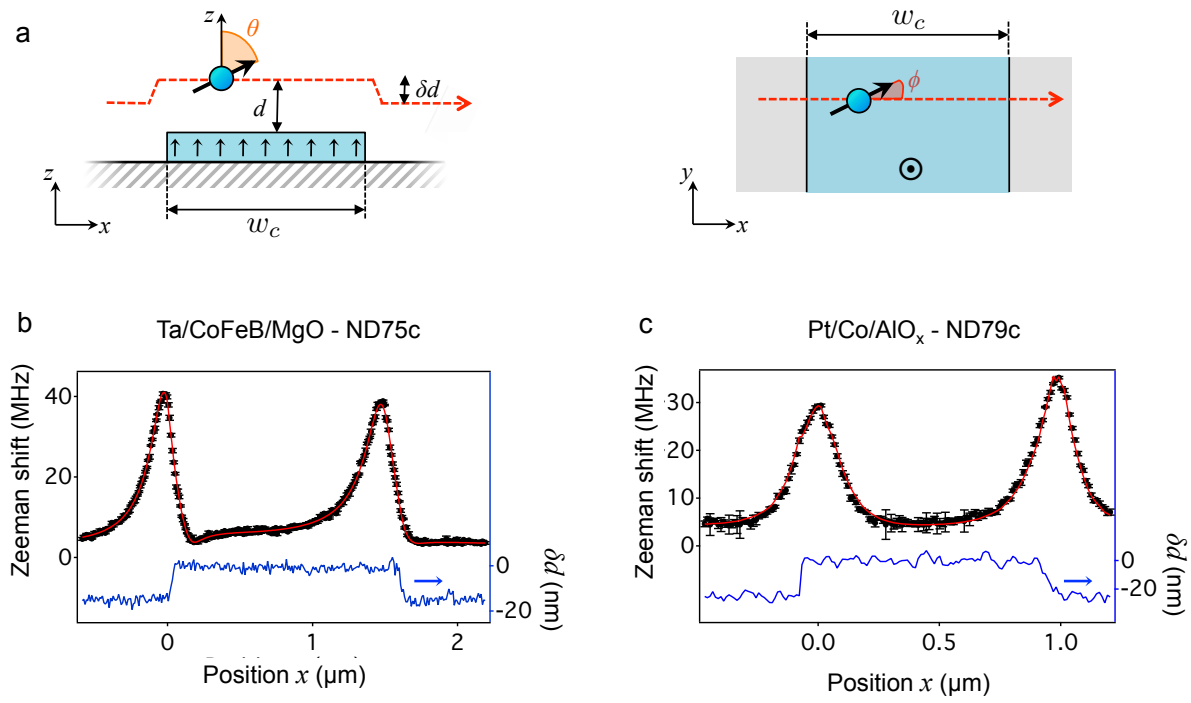

Supplementary Figure 4. Calibration of the experiment. (a) Principle of the method. The Zeeman shift $\Delta f_{\mathrm{NV}}^{\mathrm{stripe}}(x)$ is measured while scanning the NV magnetometer across a stripe of the ferromagnetic layer in the x direction. (b,c) Zeeman shift linecuts measured with ND75c across a stripe of Ta/CoFeB/MgO (b) and across a stripe of Pt/Co/AlO$_x$ with ND79c (c). The red solid line is the fit, as explained in the text. The blue curve is the topography of the sample recorded simultaneously by the AFM and used to define the distance change $\delta d(x)$ in the fit function.

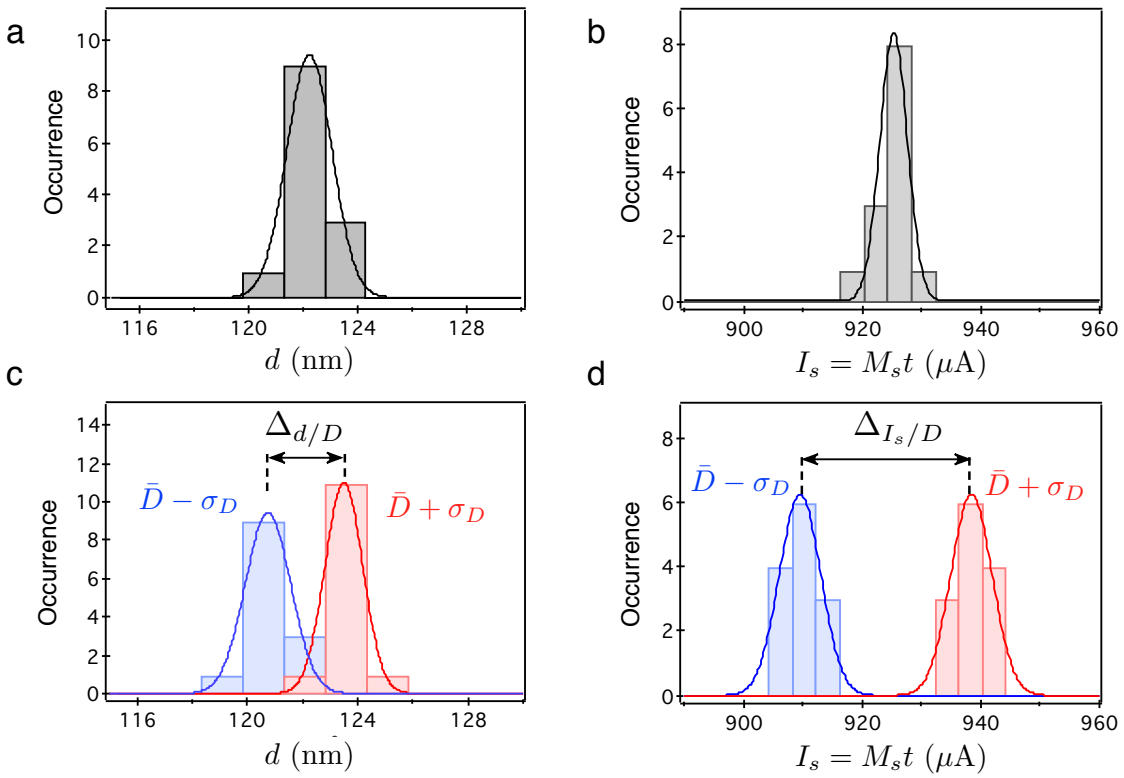

Supplementary Figure 5. Uncertainty analysis of the calibration. (a,b) Histograms of the fit outcomes for the probe-sample distance d (a) and $I_s = M_s t$ (b) obtained for a set of 13 calibration linecuts on the Ta/CoFeB/MgO sample with ND75c while fixing the parameters p_i to their nominal values $\bar{p}_i$. (c,d) Histograms of the fit outcomes with the zero-field splitting D fixed at $D = \bar{D} \pm \sigma_D$ and the other five parameters p_i fixed at their nominal values. Notations are defined in Supplementary Note 3.

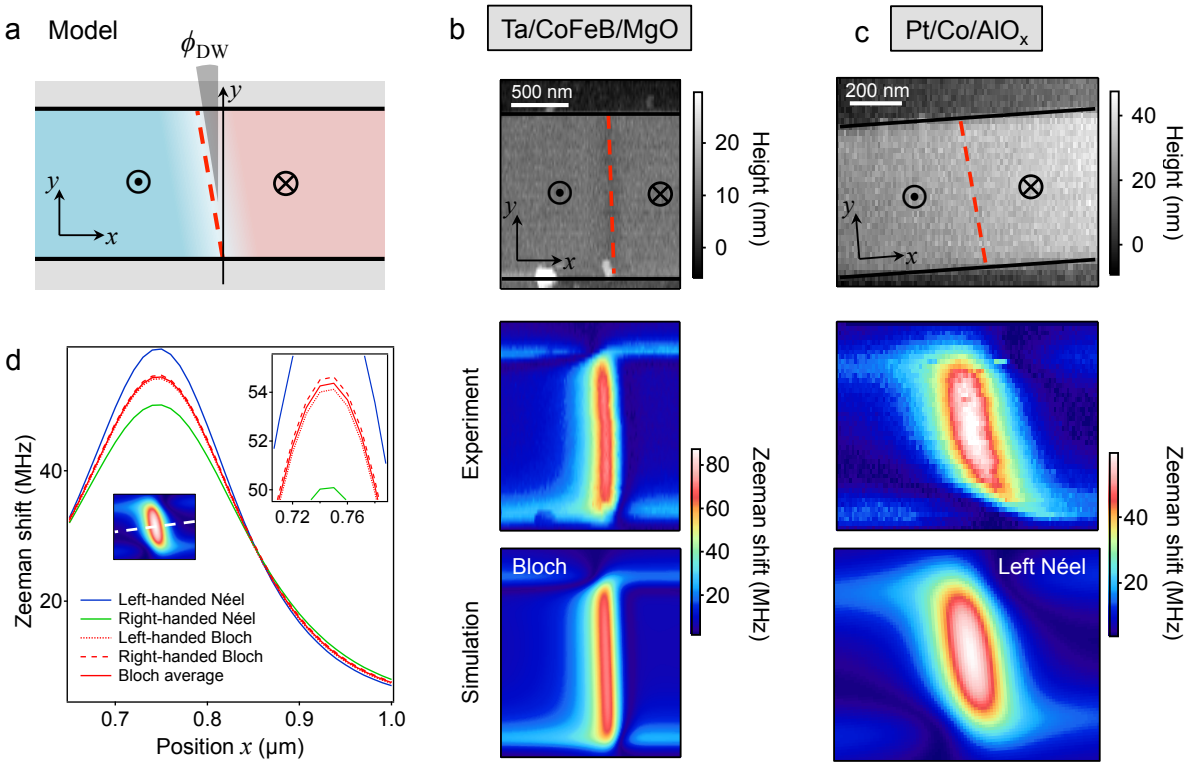

Supplementary Figure 6. Micromagnetic calculations. (a) The DW is assumed to be straight with a tilt angle ϕ_{DW} with respect to the y axis, perpendicular to the wire's long axis. (b,c) AFM image (top panel), Zeeman shift image (middle panel) and associated simulation (bottom panel) corresponding to the DW studied in (b) Fig. 2 and (c) Fig. 4 of the main paper. The simulation assumes a straight DW with $\phi_{DW} = 2°$ and $\psi = \pi/2$ in (b), and $\phi_{DW} = 6°$ and $\psi = \pi$ in (c). (d) Linecuts taken from the simulation of (c), illustrating the small effect of the chirality of the Bloch DW. Near the maximum, the field is changed by $\pm 0.5\%$ with respect to the mean value. In the case of (b), the change is even smaller ($\pm 0.3\%$).

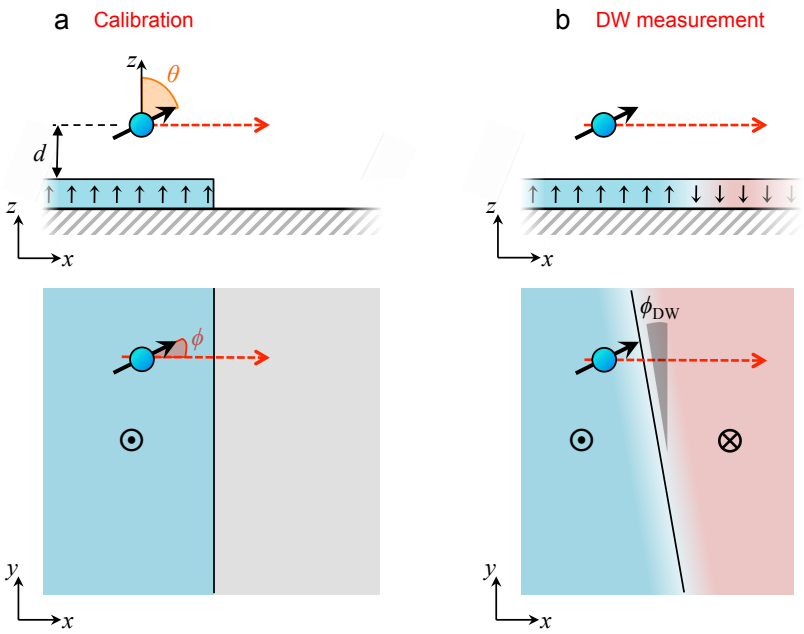

Supplementary Figure 7. Notations used to analyze the uncertainty of stray field predictions. We analyze how the error on a calibration measurement above an edge (a) and on other parameters translates into an error on the DW field (b). The calibration edge defines the (xyz) axis system. The DW is assumed to be infinitely long, with its plane tilted by an angle ϕ_{DW} with respect to the (yz) plane. The angle ψ defines the rotation of the in-plane magnetization of the DW with respect to the DW normal. Top panels: side view; Bottom panels: top view.

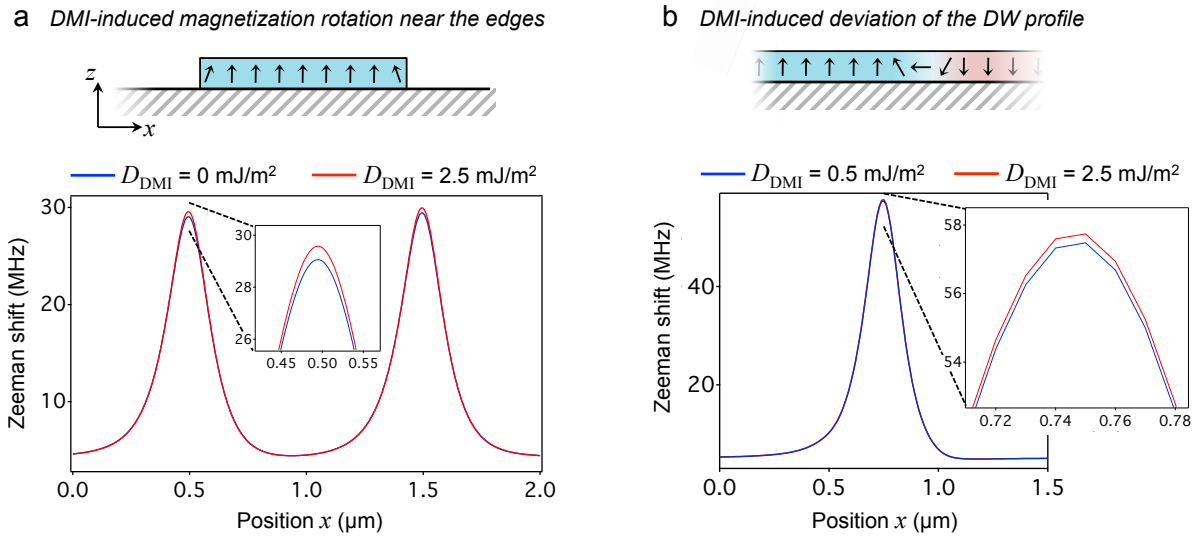

Supplementary Figure 8. Effect of a large DMI constant on stray field predictions. (a) In the presence of a strong DMI, the magnetization deviates from the out-of-plane direction near the edges of the stripe. The plot shows the Zeeman shift calculated under similar conditions as in Supplementary Figure 4(c), for two different values of D_{DMI}. (b) The DMI also makes the DW profile deviate from the profile $M_z(x) = -M_s \tanh(x/\Delta_{\mathrm{DW}})$. The plot shows the Zeeman shift calculated under similar conditions as in Fig. 4 of the main paper, for two different values of D_{DMI}.

	ND74a	ND74d	ND74e	ND74g	ND75c	ND79c
Figure	3(a)	3(b)	3(c)	3(d)	2	4
D ($\pm$0.2 MHz)	2867.1				2869.5	2866.6
E ($\pm$0.2 MHz)	3.1				3.3	4.3
θ ($\pm 2^\circ$)	99°	102°	113°	42°	62°	87°
ϕ ($\pm 2^\circ$)	-65°	27°	-81°	-7°	-25°	23°

Supplementary Table 1. Summary of the parameters (D, E, θ, ϕ) measured for the different NV center magnetometers used in this work. The second row mentions the figures of the main paper where the magnetometer is used.

(a) Ta/CoFeB/MgO with ND75c

parameter p_i	nominal value $\bar{p_i}$	uncertainty σ_{p_i}	$\epsilon_{d/p_i}(\%)$	$\epsilon_{I_s/p_i}(\%)$
w_c	1500 nm	30 nm	1.8	2.0
δd_m	17 nm	2 nm	1.0	0.2
θ	62°	2°	0.9	0.7
ϕ	−25°	2°	0.2	1.2
D	2969.5 MHz	0.2 MHz	1.0	1.6
E	3.3 MHz	0.2 MHz	0.5	0.5
$\epsilon_X = \sqrt{\epsilon_{X/\text{fit}}^2 + \sum_i \epsilon_{X/p_i}^2}$			2.5	2.9

(b) Pt/Co/AlO$_x$ with ND79c

parameter p_i	nominal value $\bar{p_i}$	uncertainty σ_{p_i}	$\epsilon_{d/p_i}(\%)$	$\epsilon_{I_s/p_i}(\%)$
w_c	980 nm	20 nm	1.8	2.0
δd_m	25 nm	3 nm	1.6	0.4
θ	87°	2°	0.2	0.1
ϕ	23°	2°	< 0.1	1.4
D	2966.6 MHz	0.2 MHz	0.8	0.8
E	4.3 MHz	0.2 MHz	< 0.1	< 0.1
$\epsilon_X = \sqrt{\epsilon_{X/\text{fit}}^2 + \sum_i \epsilon_{X/p_i}^2}$			2.9	2.6

Supplementary Table 2. Summary of the uncertainty ϵ_{X/p_i} on the value of the fit parameter X ($X = d$ and $X = I_s$) related to parameter p_i for the experiments on Ta/CoFeB/MgO with ND75c (a) and on Pt/Co/AlO$_x$ with ND79c (b). The overall uncertainty ϵ_X is estimated with Eq. (S6), assuming that all errors are independent. The standard deviations obtained from a series of 13 linecuts on Ta/CoFeB/MgO (resp. 9 linecuts on Pt/Co/AlO$_x$) are $\epsilon_{d/\text{fit}} = 0.6\%$ and $\epsilon_{I_s/\text{fit}} = 0.3\%$ (resp. $\epsilon_{d/\text{fit}} = 1.4\%$ and $\epsilon_{I_s/\text{fit}} = 0.5\%$).

(a) Ta/CoFeB/MgO with ND75c

parameter q_i	nominal value $\bar{q}_i$	uncertainty σ_{q_i}	$\epsilon_{\Theta/q_i}(\%)$
d	123 nm	3 nm	< 0.1
θ	62°	2°	< 0.1
ϕ	−25°	2°	0.2
ϕ_{DW}	2°	1°	1.1
$\epsilon_{B^\perp} = \sqrt{\epsilon^2_{B^\perp/w} + \epsilon^2_{B^{\mathrm{edge}}} + \sum_i \epsilon^2_{\Theta/q_i}}$			1.5

(b) Pt/Co/AlO$_x$ with ND79c

parameter q_i	nominal value $\bar{q}_i$	uncertainty σ_{q_i}	$\epsilon_{\Theta/q_i}(\%)$
d	118 nm	4 nm	< 0.1
θ	87°	2°	< 0.1
ϕ	23°	2°	0.4
ϕ_{DW}	6°	2°	1.1
$\epsilon_{B^\perp} = \sqrt{\epsilon^2_{B^\perp/w} + \epsilon^2_{B^{\mathrm{edge}}} + \sum_i \epsilon^2_{\Theta/q_i}}$			2.1

Supplementary Table 3. Summary of the uncertainty ϵ_{Θ/q_i} on the value of Θ related to parameter q_i for the experiments on Ta/CoFeB/MgO with ND75c (a) and on Pt/Co/AlO$_x$ with ND79c (b). The overall uncertainty $\epsilon_{B^\perp}$ is estimated with Eq. (S16), assuming that all errors are independent. The relative error on the calibration field $B^{\mathrm{edge}}_{\mathrm{NV}}(x)$ is estimated to be $\epsilon_{B^{\mathrm{edge}}} \approx 1.0\%$ in (a) and $\epsilon_{B^{\mathrm{edge}}} \approx 1.5\%$ in (b). The effect of the stripe width uncertainty leads to an additional error $\epsilon_{B^\perp/w} < 0.1\%$ in (a) and $\epsilon_{B^\perp/w} = 0.9\%$ in (b).

Supplementary Note 1. Scanning-NV magnetometry

Experimental setup. The experimental setup combines a tuning-fork-based atomic force microscope (AFM) and a confocal optical microscope (attoAFM/CFM, Attocube Systems), all operating under ambient conditions. A detailed description of the setup as well as the method to graft a diamond nanocrystal onto the apex of the AFM tip can be found in Ref.[1].

Characterization of the magnetic field sensor. The data reported in this work were obtained with NV center magnetometers hosted in three different nanodiamonds, labeled ND74 (data of Figure 3 of the main paper), ND75 (Figure 2) and ND79 (Figure 4). All nanodiamonds were ≈ 50 nm in size, as measured by AFM before grafting the nanodiamond onto the AFM tip. The magnetic field was inferred by measuring the Zeeman shift of the electron spin resonance (ESR) of the NV center's ground state [2]. This is achieved by monitoring the spin-dependent photoluminescence (PL) intensity of the NV defect while sweeping the frequency of a CW radiofrequency (RF) field generated by an antenna fabricated directly on the sample.

The Hamiltonian used to describe the magnetic-field dependence of the two ESR transitions of this $S = 1$ spin system is given by

$$\mathcal{H} = hDS_Z^2 + hE(S_X^2 - S_Y^2) + g\mu_B \mathbf{B} \cdot \mathbf{S} \ , \tag{S1}$$

where D and E are the zero-field splitting parameters that characterize a given NV center, h is the Planck constant, $g\mu_B/h = 28.03(1)$ GHz.T^{-1} [3], $\mathbf{B}$ is the local magnetic field and $\mathbf{S}$ is the dimensionless $S = 1$ spin operator. Here, the (XYZ) reference frame is defined by the diamond crystal orientation, with Z being parallel to the NV center's symmetry axis $\mathbf{u}_{\mathrm{NV}}$, as shown in Supplementary Figure 1(a).

The two ESR frequencies are denoted f_+ and f_- and the Zeeman shifts are defined by $\Delta f_\pm = f_\pm - D$ [Supplementary Figure 1(b)]. In general, $\Delta f_\pm$ are functions of $B_{\mathrm{NV},\parallel} = |\mathbf{B} \cdot \mathbf{u}_{\mathrm{NV}}|$ and $B_{\mathrm{NV},\perp} = \|\mathbf{B} \times \mathbf{u}_{\mathrm{NV}}\|$. However, in the limit of small transverse fields ($g\mu_B B_{\mathrm{NV},\perp} \ll hD$) [4], they depend only on the magnetic field projection along the NV axis $B_{\mathrm{NV},\parallel}$, following the relation

$$\Delta f_\pm(B_{\mathrm{NV},\parallel}) \approx \pm\sqrt{(g\mu_B B_{\mathrm{NV},\parallel}/h)^2 + E^2} \ . \tag{S2}$$

The parameters D and E were extracted from ESR spectra recorded at zero magnetic field using the fact that $f_\pm(\mathbf{B} = \mathbf{0}) = D \pm E$ [see Supplementary Figure 1(b,c)]. In all the data shown in this work, only the upper frequency f_+ was measured. Thereafter, we will note the corresponding

Zeeman shift $\Delta f_{\mathrm{NV}} = f_+ - D$, the subscript 'NV' reminding that it depends on the direction $\mathbf{u}_{\mathrm{NV}}$ [Supplementary Figure 1(b)]. The experimental measurements of Δf_{NV} were compared to theory by calculating the expected Zeeman shift through full diagonalization of the Hamiltonian defined by Eq. (S1), given the theoretical **B** map. However, we note that since the condition $g\mu_B B_{\mathrm{NV},\perp} \ll hD$ is usually fulfilled in our measurements, the formula (S2) is approximately valid, so that in principle one could retrieve directly the value of $B_{\mathrm{NV},\parallel}$ with good accuracy (< 0.1 mT).

The nanodiamonds were recycled several times to be used with different orientations $\mathbf{u}_{\mathrm{NV}}$ with respect to the (xyz) reference frame of the sample. The various orientations are labeled with small letters: ND74a, ND74d, ND74e, ND74g, ND75c, ND79c. The spherical angles (θ,ϕ) that characterize the direction $\mathbf{u}_{\mathrm{NV}}$ were obtained by applying an external magnetic field of known direction and amplitude with a three-axis coil system, following the procedure described in Ref. [5]. The measurement uncertainty of 2° (standard error) is related to the precision of the calibration of the coils and their alignment with respect to the (xyz) reference frame.

Supplementary Table 1 indicates the parameters D, E, θ and ϕ measured for each NV magnetometer used in this work, with the associated standard errors.

Quantitative stray field mapping. The experimental Zeeman shift maps were obtained by recording ESR spectra while scanning the magnetometer with the AFM operated in tapping mode. Each spectrum is composed of 11 bins with a bin size of 2 MHz, leading to a full range of 20 MHz. The integration time per bin is 40 ms, hence 440 ms per spectrum, that is, 440 ms per pixel of the image. As illustrated in Supplementary Figure 2, only the upper frequency f_+ is probed, and the measurement window is shifted from pixel to pixel in order to track the resonance. Each spectrum is then fitted with a Gaussian lineshape to obtain f_+ and thus Δf_{NV}. The full width at half maximum (FWHM) is typically 5-10 MHz, and the standard error on f_+ is ≈ 0.3 MHz with the above-mentioned acquisition parameters.

Supplementary Note 2. Magnetic samples

Two samples, Ta/CoFeB/MgO and Pt/Co/AlO_x, were investigated in this work. The Ta/CoFeB/MgO trilayer was deposited on a Si/SiO_2(100 nm) wafer using a PVD Timaris deposition tool by Singulus Tech. The film stack composition is Ta(5)/CoFeB(1)/MgO(2)/Ta(5), starting from the SiO_2 layer (units in nanometer). The stoichiometric composition of the as-deposited magnetic layer is $Co_{40}Fe_{40}B_{20}$. The second sample was fabricated from Pt(3)/Co(0.6)/Al(1.6) layers deposited on a thermally oxidized silicon wafer by d.c. magnetron sputtering. After deposition, the aliminium layer was oxidized by exposure to an oxygen plasma. Both samples were patterned using e-beam lithography and ion milling. A second step of e-beam lithography was finally performed in order to define a gold stripline for RF excitation, which is used to record the Zeeman shift of the NV defect magnetometer [cf. Supplementary Note 1].

Supplementary Figure 3 shows the general schematic of the samples, highlighting the regions used for calibration linecuts (stripe of width w_c) and DW measurements (stripe of width w) [cf. Supplementary Note 3]. The use of two perpendicular wires ensures that the DW is approximately parallel to the edges used for calibration. The final dimensions (height δd_m, widths w_c and w) of the patterned structures were measured with a calibrated AFM. For the Ta/CoFeB/MgO sample, $\delta d_m = 17 \pm 2$ nm and $w_c = w = 1500 \pm 30$ nm, whereas for the Pt/Co/AlO_x sample $\delta d_m = 25 \pm 3$ nm, $w_c = 980 \pm 20$ nm and $w = 470 \pm 20$ nm. The nucleation was achieved by feeding a current pulse through the gold stripline for the Ta/CoFeB/MgO sample, and by applying pulses of out-of-plane magnetic field for the Pt/Co/AlO_x sample.

Supplementary Note 3. Calibration of the experiment

Fit procedure. As discussed in the main text, a preliminary calibration of the experiment is required in order to infer the probe-sample distance d and the saturation magnetization of the sample M_s. This calibration is performed by measuring the Zeeman shift Δf_{NV} of the NV magnetometer while scanning it across a stripe of the ferromagnetic layer in the x direction, as depicted in Supplementary Figure 4(a). Since d is of the order of 100 nm in our experiments, one has $d \gg t$ where t is the thickness of the magnetic layer, so that the edges can be considered to be abrupt, *i.e.* $M_z(-w_c < x < 0) = M_s$ and $M_z = 0$ otherwise, with w_c the stripe width. In fact, due to the topography of the sample, the effective distance between the NV spin and the magnetic layer varies during the scan [see Supplementary Figure 4(a)]. This position-dependent distance can be written as $d_{\mathrm{eff}}(x) = d + \delta d(x)$, where $\delta d(x) = 0$ on average when the tip is above the stripe, and $\delta d(x) = -\delta d_m$ on average when the tip is above the bare substrate. Here δd_m is the total height of the patterned structures [cf. Supplementary Note 2]. Experimentally, one has access to the relative variations of $d_{\mathrm{eff}}(x)$ thanks to the simultaneously recorded AFM topography information, hence one can infer the function $\delta d(x)$. Therefore, only the absolute distance, characterized by d, is unknown.

The stray field components above a single abrupt edge parallel to the y direction, positioned at $x = 0$ (magnetization pointing upward for $x < 0$), are given by

$$\begin{cases} B_x^{\mathrm{edge}}(x) = \dfrac{\mu_0 M_s t}{2\pi} \dfrac{d_{\mathrm{eff}}(x)}{x^2 + d_{\mathrm{eff}}^2(x)} \\ B_y^{\mathrm{edge}}(x) = 0 \\ B_z^{\mathrm{edge}}(x) = -\dfrac{\mu_0 M_s t}{2\pi} \dfrac{x}{x^2 + d_{\mathrm{eff}}^2(x)} \ . \end{cases} \tag{S3}$$

These formulas correspond to the thin-film limit ($d \gg t$) of exact formulas, but the relative error introduced by the approximation is $< 10^{-5}$ in our case ($d/t \sim 100$), which is negligible compared with other sources of error (see below). The field above a stripe is then obtained by simply adding the contribution of the two edges, namely

$$\mathbf{B}^{\mathrm{stripe}}(x) = \mathbf{B}^{\mathrm{edge}}(x) - \mathbf{B}^{\mathrm{edge}}(x + w_c) \ . \tag{S4}$$

Using Eqs. (S3) and (S4), we obtain an analytical formula for the stray field above the stripe. A fit function $\Delta f_{\mathrm{NV}}^{\mathrm{stripe}}(x)$ is then obtained by converting the field distribution into Zeeman shift of the NV defect after diagonalization of the Hamiltonian defined by Eq. (S1), with the characteristic

parameters (θ, ϕ, E, D) of the NV magnetometer. The fit parameters are the maximum distance d and the product $I_s = M_s t$. The geometric parameters of the stripe (width w_c and height δd_m), measured independently, serve as references to rescale the length scales x and z in the linecut data before fitting. Note that in assuming an uniformely magnetized stripe, we neglect the rotation of the magnetization near the edges induced by the Dzyaloshinskii-Moriya interaction (DMI) [6]. The effect of this rotation will be discussed in Supplementary Note 5.

In the following, we focus on the experiments performed (i) with ND75c on the Ta/CoFeB/MgO sample and (ii) with ND79c on the Pt/Co/AlO_x sample, corresponding to the experimental results reported in Figures 2 and 4 of the main paper, respectively. Typical calibration linecuts are shown in Supplementary Figure 4(b,c) together with the topography of the sample. The red solid line is the result of the fit, showing a very good agreement with the experimental data.

Uncertainty analysis. Uncertainties on the fit parameters $X = \{I_s, d\}$ come from those on (i) the NV center's parameters (θ, ϕ, E, D), (ii) the geometric parameters of the stripe $(w_c, \delta d_m)$ and (iii) the fit procedure. There are therefore six independent parameters $\{p_i\} = \{\theta, \phi, E, D, w_c, \delta d_m\}$ which introduce uncertainties on the outcome of the fit. In the following, these parameters are denoted as $p_i = \bar{p_i} \pm \sigma_{p_i}$ where $\bar{p_i}$ is the nominal value of parameter p_i and σ_{p_i} its standard error. The uncertainties on θ, ϕ, E and D (resp. on w_c and δd_m) are discussed in Supplementary Note 1 (resp. in Supplementary Note 2). The nominal values and the standard errors on each parameter p_i are summarized in Supplementary Table 2.

The uncertainty and reproducibility of the fit procedure were first analyzed by fitting independent calibration linecuts while fixing the parameters p_i to their nominal values $\bar{p_i}$. As an example, the histograms of the fit outcomes for $X = \{I_s, d\}$ are shown in Supplementary Figure 5(a,b) for a set of 13 calibration linecuts recorded on the Ta/CoFeB/MgO sample with ND75c. From this statistic, we obtain $I_{s,\bar{p_i}} = 926.3 \pm 2.8$ μA and $d_{\bar{p_i}} = 122.9 \pm 0.7$ nm. Here the error bar is given by the standard deviation of the statistic. The relative uncertainty of the fit procedure is therefore given by $\epsilon_{d/\text{fit}} = 0.6\%$ for the probe-sample distance and $\epsilon_{I_s/\text{fit}} = 0.3\%$ for the product $I_s = M_s t$.

We now estimate the relative uncertainty on the fit outcomes $(\epsilon_{d/p_i}, \epsilon_{I_s/p_i})$ linked to each independent parameter p_i. For that purpose, the set of calibration linecuts was fitted with one parameter p_i fixed at $p_i = \bar{p_i} \pm \sigma_{p_i}$, all the other five parameters remaining fixed at their nominal values. The resulting mean values of the fit parameters $X = \{d, I_s\}$ are denoted $X_{\bar{p_i}+\sigma_{p_i}}$ and

$X_{\bar{p_i}-\sigma_{p_i}}$ and the relative uncertainty introduced by the errors on parameter p_i is finally defined as

$$\epsilon_{X/p_i} = \frac{X_{\bar{p_i}+\sigma_{p_i}} - X_{\bar{p_i}-\sigma_{p_i}}}{2X_{\bar{p_i}}} = \frac{\Delta_{X,p_i}}{2X_{\bar{p_i}}} \ . \tag{S5}$$

To illustrate the method, we plot in Supplementary Figure 5(c,d) the histograms of the fit outcomes while changing the zero-field splitting parameter D from $\bar{D} - \sigma_D$ to $\bar{D} + \sigma_D$. For this parameter, the relative uncertainties on d and I_s are $\epsilon_{d/D} = 1.0\%$ and $\epsilon_{I_s/D} = 1.6\%$. The same analysis was performed for all parameters p_i and the corresponding uncertainties are summarized in Supplementary Table 2. The cumulative uncertainty is finally given by

$$\epsilon_X = \sqrt{\epsilon^2_{X/\text{fit}} + \sum_i \epsilon^2_{X/p_i}} \ , \tag{S6}$$

where all errors are assumed to be independent.

Following this procedure, we finally obtain $d = 122.9 \pm 3.1$ nm and $M_s t = 926 \pm 26$ μA (or $M_s \approx 0.926$ MA.m^{-1}) for the Ta/CoFeB/MgO sample, and $d = 119.0 \pm 3.4$ nm and $M_s t = 671 \pm 18$ μA (or $M_s \approx 1.12$ MA.m^{-1}) for the Pt/Co/AlO$_x$ sample, in good agreement with the values reported elsewhere for similar samples [7-9].

Supplementary Note 4. Micromagnetic calculations

While the calibration linecuts were fitted with analytic formulas, the predictions of the stray field above the DWs were obtained using micromagnetic calculations in order to accurately describe the DW fine structure. We first used the micromagnetic OOMMF software [5,10] to obtain the equilibrium magnetization of the structure. For the Ta/CoFeB/MgO sample, the nominal values used in OOMMF are: anisotropy constant $K = 5.9 \cdot 10^5$ J.m^{-3} (obtained from the measured effective anisotropy field of 107 mT [7]), exchange constant $A = 20$ pJ.m^{-1}, film thickness $t = 1$ nm, stripe width $w = 1500$ nm, cell size $2.5 \times 2.5 \times 1$ nm^3. For the Pt/Co/AlO$_x$ sample, we used: $K = 1.3 \cdot 10^6$ J.m^{-3} (measured effective anisotropy field of 920 mT), $A = 18$ pJ.m^{-1}, $t = 0.6$ nm, $w = 470$ nm, cell size $2.5 \times 2.5 \times 0.6$ nm^3. The saturation magnetization M_s was obtained from the product $M_s t$ determined from calibration linecuts [cf. Supplementary Note 3].

We considered a straight DW with a tilt angle ϕ_{DW} with respect to the y axis. As illustrated in Supplementary Figure 6, this angle was directly inferred from the Zeeman shift images, leading to $\phi_{\mathrm{DW}} \approx 2 \pm 1^\circ$ for the DW studied in Fig. 2 of the main paper, and $\phi_{\mathrm{DW}} \approx 6 \pm 2^\circ$ for the DW studied in Fig. 4 of the main paper. The uncertainty on ϕ_{DW} enables us to account for the fact that the DW is not necessarily rigorously straight. This point will be discussed in Supplementary Note 5.

The calculation of the stray field was then performed with four different initializations of the DW magnetization: (i) right-handed Bloch, (ii) left-handed Bloch, (iii) right-handed Néel and (iv) left-handed Néel. To stabilize the Néel configuration, the DMI at one of the interfaces of the ferromagnet was added, as described in Ref. [6]. The value of the DMI parameter was set to $|D_{\mathrm{DMI}}| = 0.5$ mJ.m^{-2}, which is large enough to fully stabilize a Néel DW. The additional consequences of a stronger DMI will be discussed in Supplementary Note 5.

Once the equilibrium magnetization was obtained, the stray field distribution $\mathbf{B}(x, y)$ was calculated at the distance d by summing the contribution of all cells. Knowing the projection axis (θ,ϕ), we finally calculate the Zeeman shift map $\Delta f_{\mathrm{NV}}(x, y)$ by diagonalizing the NV center's Hamiltonian [cf. Supplementary Note 1]. Under the conditions of Figs. 2 and 4 of the main paper, the difference of stray field near the maximum between left-handed and right-handed Bloch DWs is predicted to be $< 0.5\%$ [Supplementary Figure 6(d)]. Since this is much smaller than the standard error [cf. Supplementary Note 5], we plotted the mean of these two cases, which is simply referred to as a Bloch DW, and added the deviation induced by the two possible chiralities to the displayed standard error.

Supplementary Note 5. Uncertainties of the domain wall stray field predictions

In this Section, we analyze how the uncertainties on the preliminary measurements affect the final predictions of the Zeeman shift above the DW. To keep the analysis simple and insightful, we use the approximate analytic expressions of the stray field of an infinitely long DW [Eqs. (1), (2) and (3) of the main paper]. Furthermore, we focus our attention on the positions where the DW stray field is maximum, since this is what provides information about the DW nature [see Figs. 1(c) and 1(d) of the main paper]. Finally, we use the approximation $\Delta f_{\mathrm{NV}} \approx g\mu_B B_{\mathrm{NV},\parallel}/h$ [cf. Supplementary Note 1], which is quite accurate near the stray field maximum and allows us to consider the magnetic field $B_{\mathrm{NV},\parallel}$ rather than the Zeeman shift Δf_{NV}. For clarity the subscript $\parallel$ will be dropped and the projected field will be simply denoted B_{NV}.

Out-of-plane stray field contribution $\mathbf{B}^{\perp}$. We first consider the out-of-plane contribution to the DW stray field, $\mathbf{B}^{\perp}(x)$, which is the only contribution for a Bloch structure. The stray field components above the DW can be written, in the (xyz) axis system (see Supplementary Figure 7), as

$$\begin{cases} B_x^{\perp}(x) = \dfrac{\mu_0 M_s t}{\pi} \dfrac{d\cos\phi_{\mathrm{DW}}}{\left[(x-x_{\mathrm{DW}})\cos\phi_{\mathrm{DW}}\right]^2 + d^2} \\ B_y^{\perp}(x) = \dfrac{\mu_0 M_s t}{\pi} \dfrac{d\sin\phi_{\mathrm{DW}}}{\left[(x-x_{\mathrm{DW}})\cos\phi_{\mathrm{DW}}\right]^2 + d^2} \\ B_z^{\perp}(x) = -\dfrac{\mu_0 M_s t}{\pi} \dfrac{(x-x_{\mathrm{DW}})\cos\phi_{\mathrm{DW}}}{\left[(x-x_{\mathrm{DW}})\cos\phi_{\mathrm{DW}}\right]^2 + d^2} \end{cases}, \tag{S7}$$

where x_{DW} is the position of the DW (for a given y).

We stress that this is twice the stray field above an edge of the film [see Eq. (S3)] expressed in a rotated coordinate system. Therefore, stray field measurement above the edge can be used as a reference which enables detecting any deviations from the Bloch profile. As explained below, this is a central point of the analysis.

The projection of $\mathbf{B}^{\perp}(x)$ along the NV center's axis is given by

$$B_{\mathrm{NV}}^{\perp}(x) = \left|\sin\theta\cos\phi B_x^{\perp}(x) + \sin\theta\sin\phi B_y^{\perp}(x) + \cos\theta B_z^{\perp}(x)\right| \tag{S8}$$

$$= \frac{\mu_0 M_s t}{\pi} \frac{1}{\left[(x-x_{\mathrm{DW}})\cos\phi_{\mathrm{DW}}\right]^2 + d^2} \left|d\sin\theta\cos(\phi-\phi_{\mathrm{DW}}) - (x-x_{\mathrm{DW}})\cos\phi_{\mathrm{DW}}\cos\theta\right| \tag{S9}$$

We now link $B_{\mathrm{NV}}^{\perp}(x)$ to the calibration measurement. For simplicity, we consider only one of the

two edges of the calibration stripe, *e.g.* the edge at $x = 0$. We can thus write the projected field above the edge, at a distance d, as

$$B_{\mathrm{NV}}^{\mathrm{edge}}(x) = \left|\sin\theta\cos\phi B_x^{\mathrm{edge}}(x) + \sin\theta\sin\phi B_y^{\mathrm{edge}}(x) + \cos\theta B_z^{\mathrm{edge}}(x)\right| \tag{S10}$$

$$= \frac{\mu_0 M_s t}{2\pi}\frac{1}{x^2+d^2}\left|d\sin\theta\cos\phi - x\cos\theta\right| \ . \tag{S11}$$

Comparing Eqs. (S9) and (S11), one finds the relation

$$B_{\mathrm{NV}}^{\perp}\left(\frac{x}{\cos\phi_{\mathrm{DW}}} + x_{\mathrm{DW}}\right) = 2B_{\mathrm{NV}}^{\mathrm{edge}}(x)\Theta_{d,\theta,\phi,\phi_{\mathrm{DW}}}(x) \ , \tag{S12}$$

where we define

$$\Theta_{d,\theta,\phi,\phi_{\mathrm{DW}}}(x) = \left|\frac{d\sin\theta\cos(\phi-\phi_{\mathrm{DW}}) - x\cos\theta}{d\sin\theta\cos\phi - x\cos\theta}\right| \ . \tag{S13}$$

Since $B_{\mathrm{NV}}^{\mathrm{edge}}(x)$ is experimentally measured, in principle one can use Eq. (S12) to predict $B_{\mathrm{NV}}^{\perp}(x)$ by simply evaluating the function $\Theta_{d,\theta,\phi,\phi_{\mathrm{DW}}}(x)$ as defined by Eq. (S13). As $\phi_{\mathrm{DW}} \sim 0$ implies $\Theta_{d,\theta,\phi,\phi_{\mathrm{DW}}}(x) \sim 1$, it comes that, in a first approximation, $B_{\mathrm{NV}}^{\perp}(x)$ can be obtained without the need for precise knowledge of any parameter. **In other words, the calibration measurement, performed under the same conditions as for the DW measurement, allows us to accurately predict the DW field even though those conditions are not precisely known. This is the key point of our analysis.**

Strictly speaking, $\Theta_{d,\theta,\phi,\phi_{\mathrm{DW}}}(x)$, hence $B_{\mathrm{NV}}^{\perp}(x)$, does depend on some parameters as soon as $\phi_{\mathrm{DW}} \neq 0$, namely on $\{q_i\} = \{d, \theta, \phi, \phi_{\mathrm{DW}}\}$. To get an insight into how important the knowledge of $\{q_i\}$ is, we need to examine how sensitive $\Theta_{d,\theta,\phi,\phi_{\mathrm{DW}}}(x)$ is with respect to errors on $\{q_i\}$. Owing to the sine and cosine functions in Eq. (S13), the smallest sensitivity to parameter variations (vanishing partial derivatives) is achieved when either (i) $\theta \sim 0$ (projection axis perpendicular to the sample plane) or (ii) $\theta \sim \pi/2$ (projection axis parallel to the sample plane) combined with $\phi \sim 0$ and $\phi - \phi_{\mathrm{DW}} \sim 0$. However, case (i) cannot be achieved in our experiment, because the out-of-plane RF field cannot efficiently drive ESR of a spin pointing out-of-plane. We therefore target case (ii), that is, $\theta \sim \pi/2$ and $\phi - \phi_{\mathrm{DW}} \sim 0$. For that purpose, we use a calibration edge that is as parallel to the DW as possible ($\phi_{\mathrm{DW}} \to 0$) and we seek to have a projection axis that is as perpendicular to the DW plane as possible ($\theta \to \pi/2$ and $\phi \to 0$). This is why we employ two perpendicular wires for the calibration and the DW measurements, respectively [cf. Supplementary Note 2]. Conversely, in the worst case of $\phi_{\mathrm{DW}} \sim \pi/2$ (calibration edge perpendicular to the DW)

with $\theta \sim \pi/2$, one would have $\Theta_{d,\theta,\phi,\phi_{\mathrm{DW}}}(x) \sim \phi - \phi_{\mathrm{DW}}$, directly proportional to the errors on ϕ and ϕ_{DW}.

To be more quantitative, we use Eq. (S12) to express the uncertainty on the prediction $B^{\perp}_{\mathrm{NV}}(x)$ as a function of the uncertainties on the various quantities, which gives

$$\epsilon_{B^{\perp}} = \sqrt{\epsilon^2_{B^{\mathrm{edge}}} + \sum_i \epsilon^2_{\Theta/q_i}} \ . \tag{S14}$$

Here, $\epsilon_{B^{\mathrm{edge}}}$ is given by the measurement error of $B^{\mathrm{edge}}_{\mathrm{NV}}(x)$, whereas ϵ_{Θ/q_i} is the uncertainty on $\Theta_{\{q_i\}}$ introduced by the error on the parameter $q_i \in \{d, \theta, \phi, \phi_{\mathrm{DW}}\}$, the other parameters being fixed at their nominal values, as defined by

$$\epsilon_{\Theta/q_i} = \frac{\Theta_{\bar{q_i}+\sigma_{q_i}} - \Theta_{\bar{q_i}-\sigma_{q_i}}}{2\Theta_{\bar{q_i}}} \ . \tag{S15}$$

The results are summarized in Supplementary Table 3 for the cases considered in Figs. 2 (Ta/CoFeB/MgO sample) and 4 (Pt/Co/AlO_x sample) of the main paper. ϵ_{Θ/q_i} is evaluated for $x = x_{\max}$, which is the position where the field $B^{\perp}_{\mathrm{NV}}(x)$ is maximum. It can be seen that the dominating source of uncertainty, though small ($\approx 1\%$), is the error on ϕ_{DW}, while the errors on d, θ and ϕ have a negligible impact.

In practice, to obtain the theoretical predictions shown in the main paper and in Supplementary Figure 6, we do not use explicitly Eq. (S12), but rather use the set of parameters $\{I_s, d, \theta, \phi\}$ determined following the calibration step, and put it into the stray field computation [cf. Supplementary Note 4]. This allows us to simulate more complex structures than the idealized infinitely long DW considered above, in particular the finite-width wires studied in this work. However, we stress that, as far as the uncertainties are concerned, this is completely equivalent to using Eq. (S12), since $B^{\mathrm{edge}}_{\mathrm{NV}}(x)$ is fully characterized by the set $\{I_s, d, \theta, \phi\}$ [cf. Supplementary Note 3]. The main difference comes from the influence of the edges of the wire, of width w, on the DW stray field. The standard error σ_w then translates into a relative error $\epsilon_{B^{\perp}/w}$ on the DW field $B^{\perp}_{\mathrm{NV}}$. For the Ta/CoFeB/MgO sample, $w = 1500 \pm 30$ nm, which gives a negligible error $\epsilon_{B^{\perp}/w} < 0.1\%$ for the field calculated at the center of the stripe. For the Pt/Co/AlO_x sample, the stripe is narrower, $w = 470 \pm 20$ nm, leading to $\epsilon_{B^{\perp}/w} = 0.9\%$. The overall uncertainty on the prediction $B^{\perp}_{\mathrm{NV}}$, for a DW confined in a wire, then becomes

$$\epsilon_{B^{\perp}} = \sqrt{\epsilon^2_{B^{\perp}/w} + \epsilon^2_{B^{\mathrm{edge}}} + \sum_i \epsilon^2_{\Theta/q_i}} \ . \tag{S16}$$

The overall errors are indicated in Supplementary Table 3. For Ta/CoFeB/MgO (Fig. 2 of the main paper), the overall standard error is found to be $\approx 1.5\%$, whereas for Pt/Co/AlO_x (Fig. 4) it is

$\approx 2.1\%$, in both cases much smaller than the difference between Bloch and Néel DW configurations.

We stress that the overall uncertainties are kept small ($< 3\%$) despite the fact that the uncertainties on individual parameters like the probe-to-sample distance, the NV center's axis or the saturation magnetization $M_{\rm S}$, might be larger. This is made possible thanks to the well-thought calibration strategy that avoids propagation of of those errors. The key point of this strategy is that the stray field above a Bloch DW is simply twice the stray field above the edge of the film. Therefore, the measurement above the edge serves as a reference measurement so that any deviation from the Bloch profile will be detected, without any assumption or input parameter.

In-plane stray field contribution $\mathbf{B}^{\parallel}$. According to Eq. (2) of the main paper, the in-plane contribution to the DW stray field, $\mathbf{B}^{\parallel}(x)$, is proportional to I_s and to the DW width $\Delta_{\rm DW} = \sqrt{A/K_{\rm eff}}$, where A is the exchange constant and $K_{\rm eff}$ the effective anisotropy constant. The values of A reported in the literature for Co and CoFeB thin films range from 10 to 30 pJ.m^{-1} (see *e.g.* Refs. [11,12]). Based on this range, we deduced a range for $\Delta_{\rm DW}$, namely 15-25 nm for the Ta/CoFeB/MgO sample and 4.4-7.6 nm for the Pt/Co/AlO$_x$ sample. This amounts to a relative variation $\frac{\sigma_{\Delta_{\rm DW}}}{\Delta_{\rm DW}} \approx 25\%$ around the mid-value of $\Delta_{\rm DW}$. Thus, $\epsilon_{B^{\parallel}}$ is dominated by the uncertainty on the DW width, that is, $\epsilon_{B^{\parallel}} \approx \frac{\sigma_{\Delta_{\rm DW}}}{\Delta_{\rm DW}} \approx 25\%$. All other errors can be neglected in comparison. In the micromagnetic calculations [cf. Supplementary Note 4], we used the value of A that gives the mid-value of $\Delta_{\rm DW}$, that is $A = 20$ pJ.m^{-1} for Ta/CoFeB/MgO ($\Delta_{\rm DW} = 20$ nm) and $A = 18$ pJ.m^{-1} for Pt/Co/AlO$_x$ ($\Delta_{\rm DW} = 6.0$ nm).

For an arbitrary angle ψ of the in-plane magnetization of the DW, the projected stray field writes

$$B^{\psi}_{\rm NV}(x) \;=\; B^{\perp}_{\rm NV}(x) + \cos\psi B^{\parallel}_{\rm NV}(x) \;, \tag{S17}$$

where it is assumed that $|B^{\parallel}_{\rm NV}| < |B^{\perp}_{\rm NV}|$. We deduce the expression of the absolute uncertainty for $B^{\psi}_{\rm NV}$

$$\sigma_{B^{\psi}} = \sqrt{\sigma^2_{B^{\perp}} + \cos^2\psi\sigma^2_{B^{\parallel}}} \;, \tag{S18}$$

where $\sigma_{B^{\perp}} = \epsilon_{B^{\perp}} B^{\perp}_{\rm NV}$ and $\sigma_{B^{\parallel}} = \epsilon_{B^{\parallel}} B^{\parallel}_{\rm NV}$. This is how the confidence intervals shown in Figs. 2 and 4 of the main paper were obtained. Finally, the confidence intervals for $\cos\psi$ were defined as the values of $\cos\psi$ such that the data points remain in the interval $[B^{\psi}_{\rm NV} - \sigma_{B^{\psi}} \;;\; B^{\psi}_{\rm NV} + \sigma_{B^{\psi}}]$. The

interval for the DMI parameter was deduced using the relation [13]

$$D_{\mathrm{DMI}} = \frac{2\mu_0 M_s^2 t \ln 2}{\pi^2} \cos\psi \ , \tag{S19}$$

which holds for an up-down DW provided that $|\cos\psi| < 1$.

Effects of a large DMI constant. So far, we have only considered, for simplicity and to avoid introducing additional parameters, the effect of DMI on the angle ψ of the in-plane DW magnetization. In doing so, two other effects of DMI have been neglected: (i) the DMI induces a rotation of the magnetization near the edges of the ferromagnetic structure [6] and (ii) the DW profile in the presence of DMI slightly deviates from the profile $M_z(x) = -M_s \tanh(x/\Delta_{\mathrm{DW}})$ [13]. The first (second) effect modifies the stray field above the calibration stripe (above the DW). Here we quantify these effects for the case of Pt/Co/AlO_x, for which the DMI is expected to be strong.

Recently, Martinez *et al.* have estimated that a value $D_{\mathrm{DMI}} = -2.4$ mJ.m^{-2} associated with the spin Hall effect would quantitatively reproduce current-induced DW velocity measurements in Pt/Co/AlO_x [14]. On the other hand, Pizzini *et al.* have inferred a similar value of $D_{\mathrm{DMI}} = -2.2$ mJ.m^{-2} from field-dependent DW nucleation experiments [15]. This is $\approx 70\%$ of the threshold value D_c above which the DW energy becomes negative and a spin spiral develops. Taking $D_{\mathrm{DMI}} = -2.5$ mJ.m^{-2}, we predict that the magnetization rotation at the edges reaches $\approx 20^\circ$ [6]. As a result, the field maximum above the edge is increased by $\approx 1.8\%$ under the conditions of Supplementary Figure 4(c) [see Supplementary Figure 8(a)]. This is of the order of our measurement error, so that this DMI-induced magnetization rotation cannot be directly detected in our experiment. In fitting the data of Supplementary Figure 4(b), the outcome for I_s and d is changed by a similar amount: we found $d = 119.0 \pm 3.4$ nm and $I_s = 671 \pm 18$ μA without DMI, as compared with $d = 121.0 \pm 3.4$ nm and $I_s = 670 \pm 17$ μA if $D_{\mathrm{DMI}} = -2.5$ mJ.m^{-2} is included. The difference is below the uncertainty, therefore it does not affect the interpretation of the data measured above the DW.

To quantify the second effect, we performed the OOMMF calculation with two different values of D_{DMI} that stabilize a left-handed Néel DW: $D_{\mathrm{DMI}} = -0.5$ mJ.m^{-2}, as used for the simulations shown in the main paper, and $D_{\mathrm{DMI}} = -2.5$ mJ.m^{-2}. The stray field calculations, under the same conditions as in Fig. 4 of the main paper, show an increase of the field maximum by $\approx 0.5\%$ for the stronger DMI [see Supplementary Figure 8(b)]. Again, this is well below the uncertainty of the measurements.

Besides, it is worth pointing out that these two effects tend to compensate each other, since the

first one tends to increase the estimated distance d, thereby decreasing the predicted DW field, while the second one tends instead to increase the predicted DW field. Overall, we conclude that neglecting the additional effects of DMI provides predictions for the Néel DW stray field that are correct within the uncertainty, even with a DMI constant as large as 70% of D_c. We note finally that the predictions for the Bloch case, as plotted in Fig. 2 and 4 of the main paper, are anyway not affected by the above considerations, since the Bloch case implies no DMI at all.

Supplementary References

[1] L. Rondin, *et al.*, Nanoscale magnetic field mapping with a single spin scanning probe magnetometer. *Appl. Phys. Lett.* **100**, 153118 (2012).

[2] L. Rondin, J.-P. Tetienne, T. Hingant, J.-F. Rochn P. Maletinsky, and V. Jacques, Magnetometry with nitrogen-vacancy defects in diamond. *Rep. Prog. Phys.* **77**, 056503 (2014).

[3] M. W. Doherty, F. Dolde, H. Fedder, F. Jelezko, J. Wrachtrup, N. B. Manson, L. C. L. Hollenberg, Theory of the ground-state spin of the NV^- center in diamond, *Phys. Rev. B* **85**, 205203 (2012).

[4] J.-P. Tetienne *et al.*, Magnetic-field-dependent photodynamics of single NV defects in diamond: an application to qualitative all-optical magnetic imaging. *New J. Phys.* **14**, 103033 (2012).

[5] L. Rondin *et al.*, Stray-field imaging of magnetic vortices with a single diamond spin. *Nat. Commun.* **4**, 2279 (2013).

[6] S. Rohart and A. Thiaville, Skyrmion confinement in ultrathin film nanostructures in the presence of Dzyaloshinskii-Moriya interaction. *Phys. Rev. B* **88**, 184422 (2013).

[7] T. Devolder *et al.*, Damping of $Co_xFe_{80-x}B_{20}$ ultrathin films with perpendicular magnetic anisotropy. *Appl. Phys. Lett.* **102**, 022407 (2013).

[8] N. Vernier *et al.*, Measurement of magnetization using domain compressibility in CoFeB films with perpendicular anisotropy. *Appl. Phys. Lett.* **104**, 122404 (2014).

[9] I. M. Miron *et al.*, Current-driven spin torque induced by the Rashba effect in a ferromagnetic metal layer. *Nat Mater.* **9**, 230-234 (2010).

[10] http://math.nist.gov/oommf

[11] M. Yamanouchi *et al.*, Domain structure in CoFeB thin films with perpendicular magnetic anisotropy. *IEEE Magn. Lett.* **2**, 3000304 (2011).

[12] C. Eyrich , Exchange Stiffness in Thin-Film Cobalt Alloys. *MSc Thesis* (2012, Simon Fraser University, Canada).

[13] A. Thiaville, S. Rohart, E. Jué, V. Cros, A. Fert, Dynamics of Dzyaloshinskii domain walls in ultrathin magnetic films. *Europhys. Lett.* **100**, 57002 (2012).

[14] E. Martinez, S. Emori, and G. S. D. Beach, Current-driven domain wall motion along high perpendicular anisotropy multilayers: The role of the Rashba field, the spin Hall effect, and the Dzyaloshinskii-Moriya interaction. *Appl. Phys. Lett.* **103**, 072406 (2013).

[15] S. Pizzini *et al.*, Chirality-induced asymmetric magnetic nucleation in $Pt/Co/AlO_x$ ultra-

thin microstructures. *Phys. Rev. Lett.* **113**, 047203 (2014).